


# Transition of flow field of acoustically levitated droplets with evaporation


Cite as: Phys. Fluids **31**, 102109 (2019); <https://doi.org/10.1063/1.5124499>


Submitted: 14 August 2019 . Accepted: 28 September 2019 . Published Online: 31 October 2019

Y. Sasaki (佐々木 裕哉), K. Kobayashi (小林 研仁), K. Hasegawa (長谷川 浩司) , A. Kaneko (金子 暁子), and Y. Abe (阿部 豊)

## COLLECTIONS

Paper published as part of the special topic on [Drops and Flows in Acoustic Levitation](#)

 This paper was selected as Featured

 This paper was selected as Scilight



View Online



Export Citation



CrossMark

## ARTICLES YOU MAY BE INTERESTED IN

[Multidimensional velocity fields highlight toroidal forces in acoustically levitated droplets](#)  
Scilight **2019**, 441105 (2019); <https://doi.org/10.1063/10.0000220>

[Internal flow during mixing induced in acoustically levitated droplets by mode oscillations](#)  
Physics of Fluids **31**, 112101 (2019); <https://doi.org/10.1063/1.5124988>


[Beyond the Langevin horn: Transducer arrays for the acoustic levitation of liquid drops](#)  
Physics of Fluids **31**, 101301 (2019); <https://doi.org/10.1063/1.5117335>



**NEW!**

Sign up for topic alerts

New articles delivered to your inbox



# Transition of flow field of acoustically levitated droplets with evaporation

Cite as: *Phys. Fluids* **31**, 102109 (2019); doi: [10.1063/1.5124499](https://doi.org/10.1063/1.5124499)

Submitted: 14 August 2019 • Accepted: 28 September 2019 •

Published Online: 31 October 2019



View Online



Export Citation



CrossMark

Y. Sasaki (佐々木 裕哉),<sup>1</sup> K. Kobayashi (小林 研仁),<sup>1</sup> K. Hasegawa (長谷川 浩司),<sup>2</sup>  A. Kaneko (金子 暁子),<sup>3</sup> and Y. Abe (阿部 豊)<sup>3</sup>

## AFFILIATIONS

<sup>1</sup>Graduate School of Systems and Information Engineering, University of Tsukuba, Tsukuba, Japan

<sup>2</sup>Department of Mechanical Engineering, Kogakuin University, Tokyo 163-8677, Japan

<sup>3</sup>Faculty of Engineering, Information and Systems, University of Tsukuba, Tsukuba, Japan

**Note:** This paper is part of the Special Topic on Drops and Flows in Acoustic Levitation.

## ABSTRACT

We investigated the multidimensional velocity field of acoustically levitated droplets using stereoscopic particle image velocimetry. To clarify the correlation between evaporation behavior and internal and external flows, binary droplets of ethanol and water were used as test fluids. Immediately following droplet levitation, toroidal vortices were generated in the droplet; however, the internal flow transitioned to uniaxial rotational flow as the ethanol component evaporated. In the external flow field, initially, the flow direction was distant from the top and bottom of the droplet with circulating vortices near the droplet surface. As evaporation progressed, the external flow direction transitioned to the opposite direction as the circulation vortices expanded. To investigate the driving force of the uniaxial rotation of the levitated droplet, we simulated the internal flow of the rotating droplet. The simulation and experimental results were in good agreement relative to the order and distribution profile of the flow velocity. Based on these results, we consider the transition mechanism of internal and external flow structures of acoustically levitated droplets with evaporation. Our experimental and simulation results provide deeper physical insights into noncontact fluid manipulation and indicate potential future applications.

© 2019 Author(s). All article content, except where otherwise noted, is licensed under a Creative Commons Attribution (CC BY) license (<http://creativecommons.org/licenses/by/4.0/>). <https://doi.org/10.1063/1.5124499>

## I. INTRODUCTION

Containerless processing and fluid manipulation in midair using levitation technology, such as the acoustic levitation method (ALM), has been attracting attention. The ALM can suspend micrometer to millimeter sized droplets near the pressure node of an acoustic standing wave.<sup>1–3</sup> The ALM uses relatively simple instruments compared to electrostatic and magnetic levitation that constrain the physical properties of suspended samples.<sup>4</sup> In addition, the ALM has been applied in material science, analytical chemistry, and pharmaceutical science fields because, with the ALM, samples are not subject to the effects of container walls, which can cause contamination and heterogeneous nucleation.<sup>5–9</sup>

Recently, the ALM has been applied to manipulating levitated objects using an ultrasonic phased array,<sup>10–13</sup> and realization of complete containerless processing using the ALM is anticipated.

However, when handling fluids in midair with the ALM, various phenomena, such as interfacial deformations and atomization, occur in the droplets due to unavoidable nonlinear effects.<sup>14–18</sup> In addition, it has been demonstrated that the characteristic flows that occur inside and outside acoustically levitated droplets<sup>19–28</sup> enhance the heat<sup>29,30</sup> and mass transfer<sup>31–39</sup> of droplets. For complete containerless processing and manipulation of levitated samples using the ALM, better understanding of such nonlinear phenomena is important.

To investigate the correlation of internal and external flows of acoustically levitated droplets, Zhao *et al.* conducted numerical analyses under the assumption that the flow in the test section is steady and axisymmetric. In addition, it was suggested that the circulation flows in the Stokes layer near the droplet interface determine the structures of the internal and external flows.<sup>19</sup> Rednikov *et al.* analyzed the flow structure in the Stokes layer during deformation of

the floating droplet and displacement from the node of the acoustic standing wave.<sup>20,21</sup> However, the flow structures differed from theoretical predictions.<sup>23–27,34,35</sup> Previous studies clarified the correlation between flows of acoustically levitated droplet and the phase change behavior. Kobayashi *et al.*<sup>34</sup> visualized the external flow and concentration field of an evaporating droplet in a single acoustic levitator using an interferometer and particle tracking velocimetry (PTV) to clarify the effect of saturated vapor pressures of the droplet on the external flow field. In addition, Hasegawa *et al.*<sup>24–26,35</sup> conducted particle image velocimetry (PIV) measurements on premixed droplets of ethanol and water. They demonstrated experimentally that the internal and external flow structures change with evaporation of the levitated droplet. However, existing flow visualization experiments have primarily dealt with two-dimensional flow fields on a cross section of the droplet. Although visualization and quantification of three-dimensional flow fields is scientifically and practically important, three-dimensional analysis of the internal and external flows of acoustically levitated droplets has not been performed to date.

This paper presents the flow dynamics of acoustically levitated droplets to clarify the correlation between internal and external flows of acoustically levitated droplets under phase change behavior. To clearly characterize the behavior of the droplet, we performed three-dimensional visualization measurements of the velocity field of the levitated droplet using stereoscopic PIV (stereo PIV). For a binary droplet of ethanol and water, both the internal and external flow structures transition as evaporation progresses. In addition, to gain deeper physical insight into the relation between internal and external flows, we simulated the three-dimensional internal flow structure of a rotating droplet with a constant angular velocity according to the theory proposed by Sano.<sup>40</sup> Based on the experimental and simulation results, we considered the transition process of internal and external flow structures and the effect of rotation on an acoustically levitated droplet with evaporation. We believe that our investigation will stimulate further experimental, theoretical, and numerical studies. The droplet levitation dynamics associated with flow fields and phase change reported herein may provide more universal understanding relative to practical applications, such as microreactors<sup>41</sup> and acoustic tweezers.<sup>42</sup>

## II. EXPERIMENTAL METHOD AND CONDITIONS

### A. Acoustic levitation

Figure 1 is a schematic of the sound field levitation system used in this study. This device comprises a test unit that levitates droplets and peripheral equipment. The sine wave signal was generated from the function generator and amplified by the amplifier. The sound wave emitted from the horn was reflected by the reflector to form an acoustic standing wave in the test section. The sample was injected using a syringe near the sound pressure node, and the droplet was suspended in midair. The volume equivalent droplet diameter was varied between 2.44 and 2.50 mm. The distance between the horn and reflector was 47.5 mm, which is equivalent to approximately 2.5 wavelengths. The resonance frequency of the ultrasonic waves was 19.4 kHz, which means the wavelength was approximately 19 mm at room temperature.

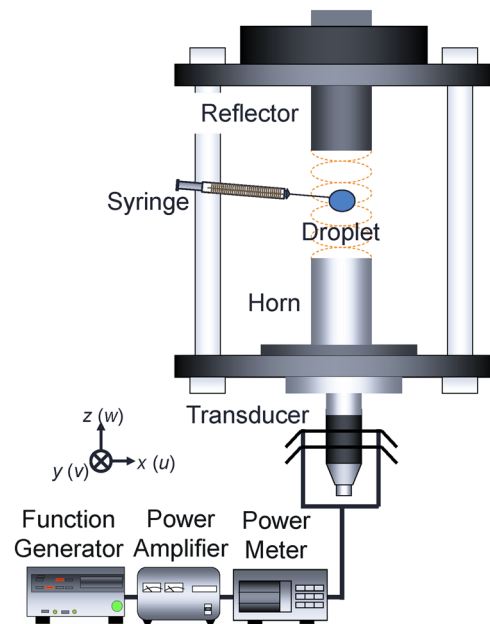


FIG. 1. Acoustic levitation apparatus.

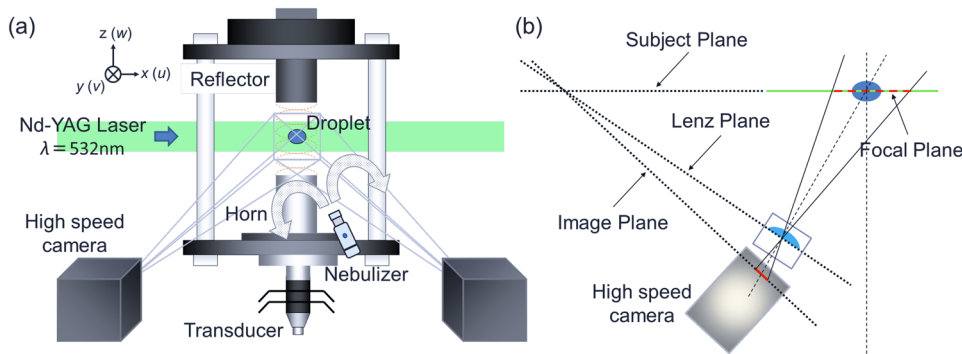
### B. Stereo PIV

Figure 2 shows the system used to perform simultaneous stereo measurement of the internal and external flows of an acoustically levitated droplet. Figure 2(a) is a schematic diagram of the stereo measurement system. Water mist (diameter  $5\ \mu\text{m}$ ) was produced by a nebulizer as tracer particles to visualize an external flow. To visualize an internal flow, a levitated sample was premixed with silver-coated particles (DANTEC, S-HGS-10, average diameter:  $10\ \mu\text{m}$ ) as tracer particles. The vertical cross section of a levitated droplet was illuminated using a sheet laser (Japan Laser Co., DPGL-5W-L), and the internal flow field of the droplet was simultaneously measured from two sides of the droplet using two high-speed cameras (Photron, FASTCAM Mini AX-200). These flow fields were recorded at 500 frames per second. To apply stereo PIV using two cameras, the right and left cameras must be placed symmetrically with respect to the normal plane of the target object. Therefore, it is not possible to focus on the entire target area (levitated droplet and surrounding external flow field) due to the restricted depth of field. To address this technical problem, we applied the Scheimpflug theorem<sup>43</sup> by placing the lens plane and the image plane nonparallelly, as shown in Fig. 2(b). By adapting this theorem, we successfully observed stereoscopic images of both the internal and external flows of the levitated droplet simultaneously.

Table I shows the physical properties of the test fluids used in our experiment (water and ethanol) at  $T = 300\ \text{K}$ .

### C. Vortex thickness measurement method

We used PTV to investigate the circulating vortices near the interface of the levitated droplet. Figure 3 illustrates the method



**FIG. 2.** Schematic of stereo measurement system: (a) simultaneous measurement of internal and external flows of levitated droplets and (b) Scheimpflug theorem.

**TABLE I.** Physical properties of test fluids at 300 K.<sup>44</sup>

| Sample  | $M$ (g/mol) | $P_{sat}$ (Pa) | $\rho_L$ (kg/m <sup>3</sup> ) | $\nu_L$ (mm <sup>2</sup> /s) | $\rho_G$ (kg/m <sup>3</sup> ) | $\nu_G$ (mm <sup>2</sup> /s) | $\sigma$ (mN/m) |
|---------|-------------|----------------|-------------------------------|------------------------------|-------------------------------|------------------------------|-----------------|
| Water   | 18          | 3537           | 996.5                         | 0.86                         | 0.0256                        | 81.39                        | 71.69           |
| Ethanol | 46          | 8841           | 783.8                         | 1.34                         | 1.92                          | 4.60                         | 21.50           |

used to measure the thickness of the circulating vortex near the droplet interface. First, multiple exposure processing was performed on 15 arbitrary image groups ( $\Delta t$ : every 30 ms) and an image depicting particle trajectories were acquired. The coordinates of the center of the droplet were determined by an elliptical approximation, as shown in Fig. 3. Next, a half line was drawn from the center of the droplet to the outer edge of the circulating vortex via the droplet interface. The intersection of the half line, the interface, and the outer edge of the circulating vortex was defined as the thickness of the circulating vortex. We measured each case five times, and the average thickness was obtained.

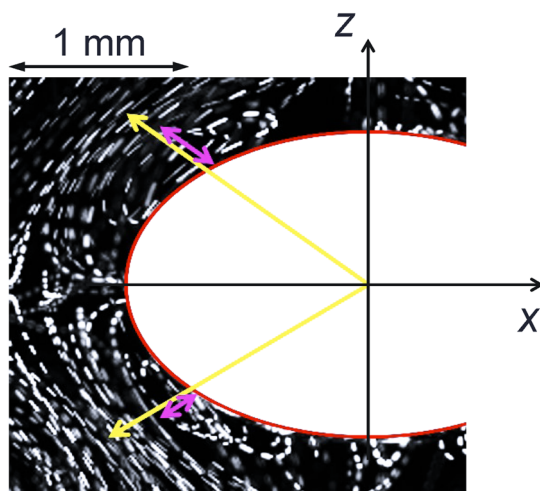


**FIG. 3.** Measurement method for vortex thickness in the vicinity of the droplet.

### III. RESULTS

#### A. Experiment: Internal and external flow structure of droplet

By applying stereo PIV to 50 wt. % ethanol droplets, we visualized and measured the transition process of the internal and external flow structure due to the progress of evaporation.

##### 1. Internal flow

Figure 4 visualizes the transition process of the internal flow structure of 50 wt. % ethanol droplets. As can be seen, the toroidal vortices, which are symmetrical in the vertical and horizontal plane (shown by the pink arrows), were generated in the droplet immediately after levitation ( $t = 0$  s). In terms of the toroidal vortex structure, the stagnation point of the vortex center was displaced to the side of the droplet ( $t = 30$  s) and completely disappeared ( $t = 50$  s). After the flow transition shown in Figs. 4(a)–4(c), upward flow in the  $z$  direction in the upper part of the droplet and downward flow in the  $z$  direction in the lower part of the droplet developed gradually ( $t = 75$  s). Finally, the internal flow structure transitioned to a rotational flow with a single rotation axis ( $t = 100$  s). Based on the visualization measurements of the internal flow of droplets in earlier studies,<sup>24,34,35</sup> the flow structures shown in Figs. 4(a) and 4(e) are the same as those of levitated pure ethanol and water droplets, respectively. In other words, as the evaporation proceeds, the toroidal vortex structure (similar to that in the pure ethanol droplet case) finally shifted to a rotational flow structure (similar to a pure water droplet).

##### 2. External flow

Figure 5 visualizes the transition process of the external flow structure of 50 wt. % ethanol droplets. Via multiple exposure processing, the flow direction is visualized and represented by pink and

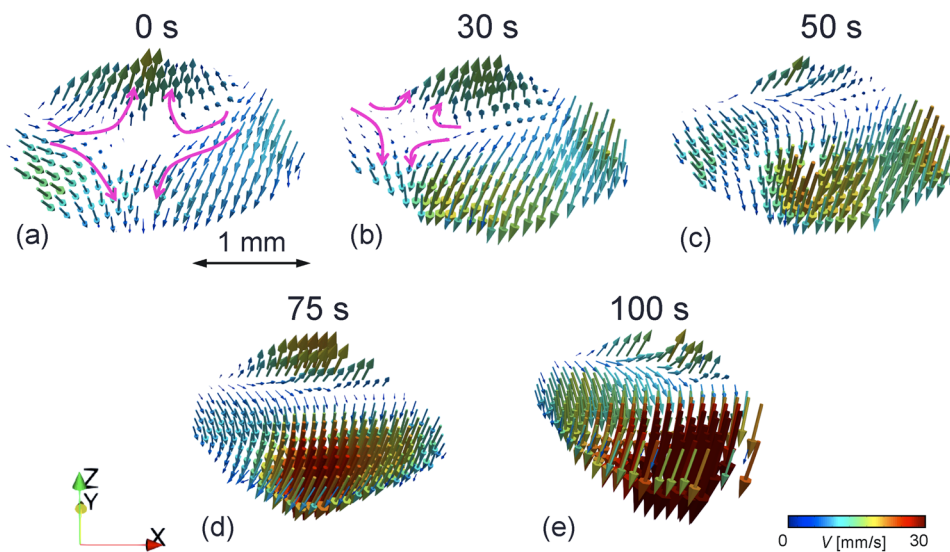


**FIG. 4.** Transition of internal flow structure of 50 wt. % ethanol droplet. (a) Immediately after stable levitation ( $t = 0$  s), (b)  $t = 30$  s, (c)  $t = 50$  s, (d)  $t = 75$  s, and (e)  $t = 100$  s.

blue arrows at  $t = 0$  s, 125 s, and  $t = 250$  s. In Fig. 5(a) (Multimedia view), the flow directions were toward the droplet (shown by the pink arrows at the top and bottom of the droplet) immediately after stable levitation ( $t = 0$  s), and circular vortices (blue arrows) appeared simultaneously at the upper and lower edges of the droplet. With the evaporation of the levitated volatile droplets, it was confirmed that the circulating vortices (blue arrows) expanded gradually and the external flow structure transitioned to that in Fig. 5(c) (Multimedia view). It is considered that this was caused by the dynamic viscosity of the gas phase around the droplet changing as the evaporation amount of ethanol decreased gradually.

Figure 6 shows the thickness of these circular vortices (Sec. II C) based on the result shown in Fig. 5. In Fig. 6, the horizontal axis represents elapsed time from the start of stable floating, and the vertical axis represents the thickness of the circulating vortex. The plots in Fig. 6 show the thickness of the circulating vortices generated at the top (●) and bottom (■) of the droplet, respectively. As can be seen, immediately after droplet levitation, the thickness of the circulating vortex increased relatively slowly until  $t = 100$  s. In contrast, it increased rapidly after  $t = 100$  s. For the droplet evaporation, Hasegawa *et al.*<sup>35</sup> experimentally demonstrated that the evaporation rate of the ethanol/water mixture in an acoustic field

exhibited two distinct stages, i.e., preferential evaporation by ethanol and evaporation by water. In addition, Kobayashi *et al.*<sup>34</sup> observed that the thickness of the circular vortex corresponds to the gas phase concentration around the droplet. Based on these results, we can conclude that the clear expansion of the circular vortex thickness can be caused by the decrease and the diffusion of the concentration of the ethanol vapor around the droplet after approximately  $t = 100$  s.

To better understand the external flow field, the length scale of the upper and lower circular vortices were compared. The upper vortex was clearly thicker than the lower vortex due to the levitation position of the droplet. In a ground gravity environment, an acoustically levitated droplet can be suspended slightly below the pressure node of the acoustic standing wave due to the effect of the gravity. The acoustic pressure exerted on the bottom of the droplet interface is stronger than that on the top. Therefore, symmetry breaking of the external flow structure is likely to occur.

## B. Numerical simulation: Internal flow

In Sec. III A, we described the visualization results of the transition process of the internal and external flow structures of

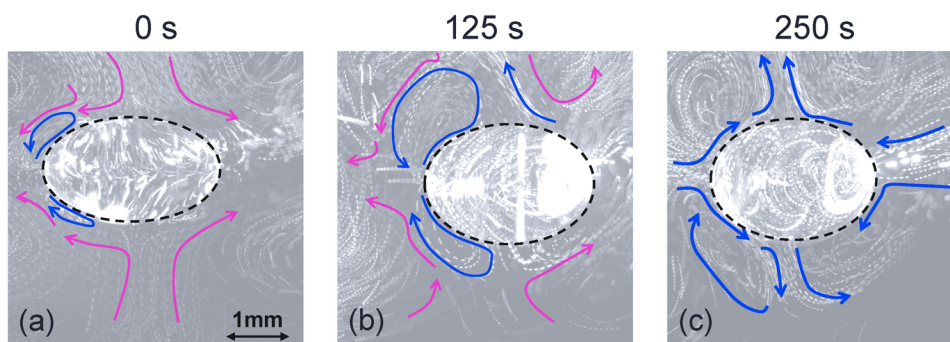


**FIG. 5.** Transition of an external flow structure of 50 wt. % ethanol droplet. Pink and blue arrows indicate the external flow structure and the circular vortex, respectively. (a) Immediately after stable levitation ( $t = 0$  s), (b)  $t = 125$  s, and (c)  $t = 250$  s. Multimedia views: (a) and (c) <https://doi.org/10.1063/1.5124499.1>; <https://doi.org/10.1063/1.5124499.2>

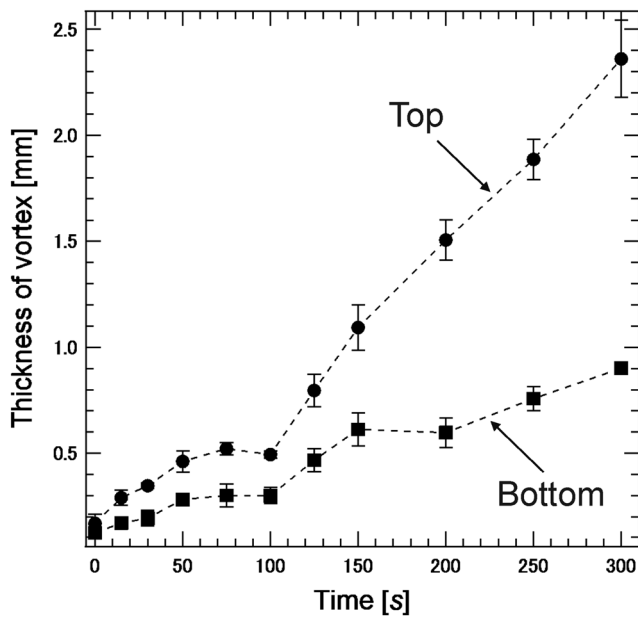


FIG. 6. Thickness of vortices around the 50wt. % ethanol droplet.

50 wt. % ethanol droplets. For the volatile droplet (ethanol), it was suggested that a pair of vortex is formed in the levitated droplet. For the less volatile droplet (water), it was confirmed that a rotating flow structure with a single rotation axis was generated inside the droplet. This uniaxial rotation may be caused by the rotational torque on the droplet interface because of the external flow, but the driving force remains unclear. Thus, to evaluate the effect of rotational torque, we three-dimensionally simulated the flow generated inside the droplet given constant rotational angular velocity by rotational torque. Then, we compared the simulated internal flow field to the experimental data obtained by stereo PIV.

### 1. Problem statement and calculation conditions

We analyzed the flow inside the rotated droplet based on the equation of continuity and the Navier-Stokes (NS) equation by Sano.<sup>40</sup> Assuming the droplet rotates at constant angular velocity  $\omega$  with external torque, the equation of continuity and the NS equation in rotating spherical coordinates are given as follows:

$$\frac{1}{r^2} \frac{\partial}{\partial r} (r^2 v_r) + \frac{1}{r \sin \theta} \frac{\partial}{\partial \theta} (\sin \theta v_\theta) = 0, \quad (1)$$

$$\Delta v_r - \frac{2}{r^2} v_r - \frac{2}{r^2} \frac{\partial v_\theta}{\partial \theta} - \frac{2v_\theta}{r^2} \cot \theta - \frac{\partial p}{\partial r} = Re \left( v_r \frac{\partial v_r}{\partial r} + \frac{v_\theta}{r} \frac{\partial v_r}{\partial \theta} - \frac{v_\theta^2 + v_\theta^2}{r} \right), \quad (2)$$

$$\Delta v_\theta - \frac{v_\theta}{r^2 \sin^2 \theta} + \frac{2}{r^2} \frac{\partial v_r}{\partial \theta} - \frac{1}{r} \frac{\partial p}{\partial \theta} = Re \left( v_r \frac{\partial v_\theta}{\partial r} + \frac{v_\theta}{r} \frac{\partial v_\theta}{\partial \theta} + \frac{v_r v_\theta}{r} - \frac{v_\theta^2 \cot \theta}{r} \right), \quad (3)$$

TABLE II. Calculation conditions.

|   |                          |
|---|--------------------------|
| Equivalent Volume radius $a$ (mm)                             | 1.44                     |
| Representative flow velocity $U$ (mm/s)                       | 20.8                     |
| Angular velocity $\omega$ (rad/s)                             | 14.4                     |
| Kinematic viscosity $\nu_{water}$ ( $10^6$ m <sup>2</sup> /s) | 1.004                    |
| $x, y, z$ mesh length (mm)                                    | -1.0 to 1.0              |
| Number of meshes ( $x \times y \times z$ )                    | $20 \times 20 \times 20$ |

$$\Delta v_\theta - \frac{v_\theta}{r^2 \sin^2 \theta} = Re \left\{ v_r \frac{\partial v_\theta}{\partial r} + \frac{v_\theta}{r} \frac{\partial v_\theta}{\partial \theta} + \frac{v_\theta v_\theta \cot \theta}{r} + \frac{2}{Ro} (v_r \sin \theta + v_\theta \cos \theta) \right\}, \quad (4)$$

where

$$\Delta = \frac{1}{r^2} \frac{\partial}{\partial r} \left( r^2 \frac{\partial}{\partial r} \right) + \frac{1}{r^2 \sin \theta} \frac{\partial}{\partial \theta} \left( \sin \theta \frac{\partial}{\partial \theta} \right), \quad (5)$$

$$Re = \frac{Ua}{\nu}, \quad Ro = \frac{U}{\omega a}. \quad (6)$$

Here,  $\Delta$  is Laplacian,  $Re$  and  $Ro$  are the Reynolds and Rossby numbers, respectively,  $a$  is the radius of the droplet, and  $\nu$  is the kinematic viscosity. We solve these governing equations according to Sano's proposition. It is assumed to be a steady and axisymmetric flow field. Thus, differentiation relative to time  $t$  and azimuthal angle  $\varphi$  is negligible. It is also assumed that the droplet stays spherical, velocity and stress are continuous under the no slip condition on the surface of the droplet, and  $Re$  is sufficiently small such that it can be solved with the second-order [ $O(Re^2)$ ] solutions using a perturbation procedure. Table II shows the simulation conditions. Compared to the simulation results for the experimental one, we substituted the experimental data for the water droplet shown in Fig. 7 to determine the parametric conditions for this simulation. Here, an equivalent volume radius and maximum internal velocity, which we obtained from our experiment, were used for  $a$  and flow velocity  $U$ . Note that angular velocity  $\omega$  was derived from  $U$  divided by  $a$ .

### 2. Patterns of internal flow

The leading-order [ $O(Re^0)$ ] solutions are obtained as follows:

$$v_r^{(0)} = v_\theta^{(0)} = 0, \quad (7)$$

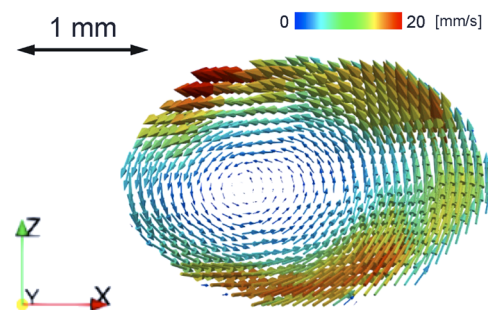


FIG. 7. Experimental result of water droplet.

$$v_{\theta}^{(0)} = \frac{1}{Ro} r \sin \theta, \quad \text{for } r \leq a. \quad (8)$$

Equation (8) shows that velocity  $v_{\theta}$  in the circumferential direction increases in proportion to radius  $r$  in an arbitrary horizontal section with the same zenith angle  $\theta$ . In other words, a solution in the order  $O(Re^0)$  indicates that the droplet undergoes complete rigid body rotation.

The basic equations of the next order [ $O(Re^1)$ ] are given as follows:

$$\frac{1}{r^2} \frac{\partial}{\partial r} (r^2 v_r^{(1)}) + \frac{1}{r \sin \theta} \frac{\partial}{\partial \theta} (\sin \theta v_{\theta}^{(1)}) = 0, \quad (9)$$

$$\Delta v_r^{(1)} - \frac{2}{r^2} v_r^{(1)} - \frac{2}{r^2} \frac{\partial v_{\theta}^{(1)}}{\partial \theta} - \frac{2v_{\theta}^{(1)}}{r^2} \cot \theta - \frac{\partial p^{(1)}}{\partial r} = -\frac{1}{r} (v_{\theta}^{(0)})^2, \quad (10)$$

$$\Delta v_{\theta}^{(1)} - \frac{v_{\theta}^{(1)}}{r^2 \sin^2 \theta} + \frac{2}{r^2} \frac{\partial v_r^{(1)}}{\partial \theta} - \frac{1}{r} \frac{\partial p^{(1)}}{\partial \theta} = -\frac{\cot \theta}{r} (v_{\theta}^{(0)})^2, \quad (11)$$

$$\Delta v_{\theta}^{(1)} - \frac{v_{\theta}^{(1)}}{r^2 \sin^2 \theta} = 0. \quad (12)$$

With Eq. (12), only  $\Delta v_{\theta}^{(1)} = 0$  is regular at the droplet center and zero at the interface. In addition, among the homogeneous solutions in Eqs. (9)–(11), those that are bounded inside the droplet and become 0 at the interface with the solution's symmetry are given as follows:

$$v_r^{(11)} = 2A(1 - r^2) \cos \theta, \quad v_{\theta}^{(11)} = -2A(1 - 2r^2) \sin \theta, \quad v_{\theta}^{(11)} = 0, \quad (13)$$

$$\begin{aligned} v_r^{(12)} &= 4Br(1 - r^2)P_2(\cos \theta), \\ v_{\theta}^{(12)} &= -Br(3 - 5r^2) \sin 2\theta, \quad v_{\theta}^{(12)} = 0. \end{aligned} \quad (14)$$

Figure 8 shows the streamlines in the vertical section of the droplet based on Eqs. (13) and (14). Figures 8(a) and 8(b) reproduce a pair of vertically and horizontally symmetrical vortices and two pairs of vortices. Based on this analysis, the flow structures in Figs. 8(a) and 8(b) are defined as one-cell and two-cell types in this present study. Here, the first superscripts in Eqs. (13) and (14) represent the order  $Re$  (0, 1, or 2), and the second superscripts represents the cell type (one-cell or two-cell). In addition, in Eqs. (13) and (14),  $A$  and  $B$  are arbitrary constants that identify the strength of the one-cell and two-cell modes, respectively. We determined arbitrary constant  $A$  based on the experimental results of the internal flow of the water droplet by stereo PIV (Fig. 7). Therefore,  $A$  was determined by substituting the experimental value of  $v_{\theta}$  at  $r = a$ ,  $\theta = \pi/2$  in the second equation in Eq. (13). Note that the fitting parameter  $B$  was varied in each simulation.

Next, the second-order  $O(Re^2)$  solutions for the one-cell and two-cell types are obtained as follows:

$$v_r^{(2)} = v_{\theta}^{(2)} = 0, \quad (15)$$

$$v_{\theta}^{(21)} = -\frac{4A}{7Ro} r^2 (1 - r^2) \sin \theta \cos \theta, \quad (16)$$

$$v_{\theta}^{(22)} = \frac{B}{Ro} r \sin \theta \left\{ \frac{2}{5} - \frac{16}{15} r^2 + \frac{2}{3} r^4 - \frac{4}{9} r^2 (1 - r^2) \cos 2\theta \right\}. \quad (17)$$

For  $O(Re^2)$ , the velocity of the vertical component become 0 [same as the solution of the order  $O(Re^0)$ ], and only the velocity of the circumferential component exists. Finally, the internal flow of a droplet rotated with constant angular velocity is obtained as follows:

$$v_{theory} = v^{(0)} + Re(v^{(11)} + v^{(12)}) + Re^2(v^{(21)} + v^{(22)}). \quad (18)$$

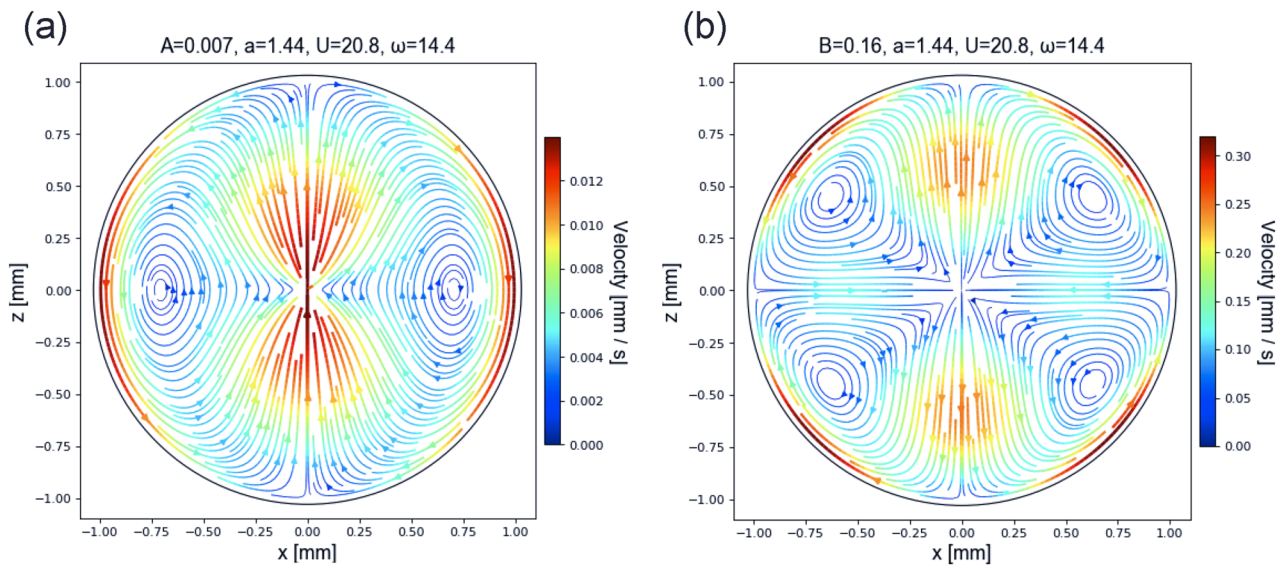
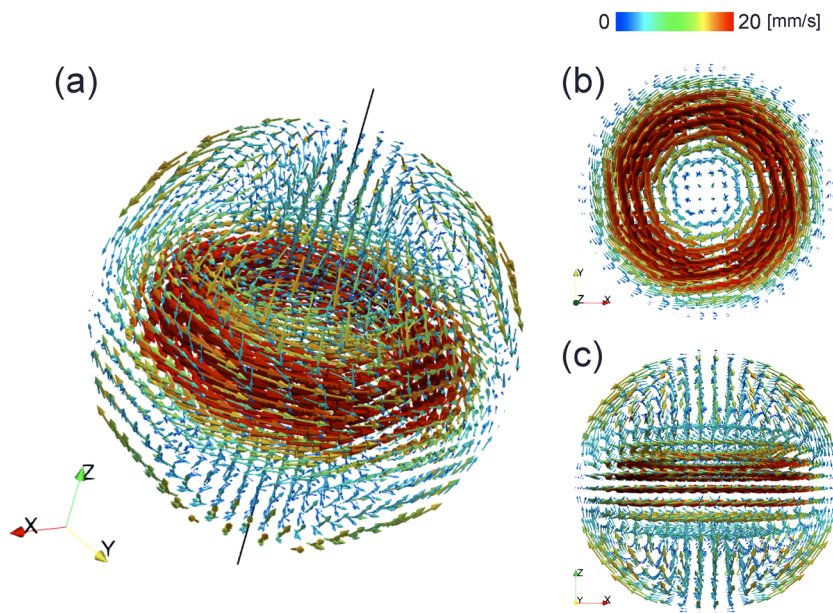


FIG. 8. Streamlines in the vertical section of the droplet when  $a = 1.44$ ,  $U = 20.8$ , and  $\omega = 14.4$ : (a) one-cell type flow structure when  $A = 0.007$  and (b) two-cell type flow structure when  $B = 0.16$ .



**FIG. 9.** Simulation of internal flow of a rotational droplet when  $a = 1.44$  mm,  $U = 20.8$  mm/s,  $\omega = 14.4$  rad/s,  $A = 0.007$ , and  $B = 0.16$ : (a) bird's-eye view, (b) top view, and (c) side view. Multimedia view: (a) <https://doi.org/10.1063/1.5124499.3>

Based on Eq. (18), Fig. 9 shows the three-dimensional simulation of the internal flow under the calculation conditions shown in Table II. Figure 9(a) (Multimedia view) shows a bird's-eye view. Figures 9(b) and 9(c) show top and side views, respectively. As shown in Fig. 9(a) (Multimedia view), the velocity of the circumferential component was relatively large near the equatorial plane. Figure 9(b) shows that a rotational flow with a single axis occurred in the circumferential direction of the droplet. In Fig. 9(c), although the flow velocity is relatively smaller than the flow velocity in the circumferential

direction observed in Fig. 9(b), vertical and horizontal symmetrical convection occurred in the vertical section. Thus, we have successfully demonstrated one-cell and two-cell type flows in our numerical simulation.

### 3. Comparison of experimental results

We compared the above simulation results to those obtained for the water droplet via stereo PIV. Figure 10 shows the velocity component  $v_\theta$  as a function of the normalized distance from the

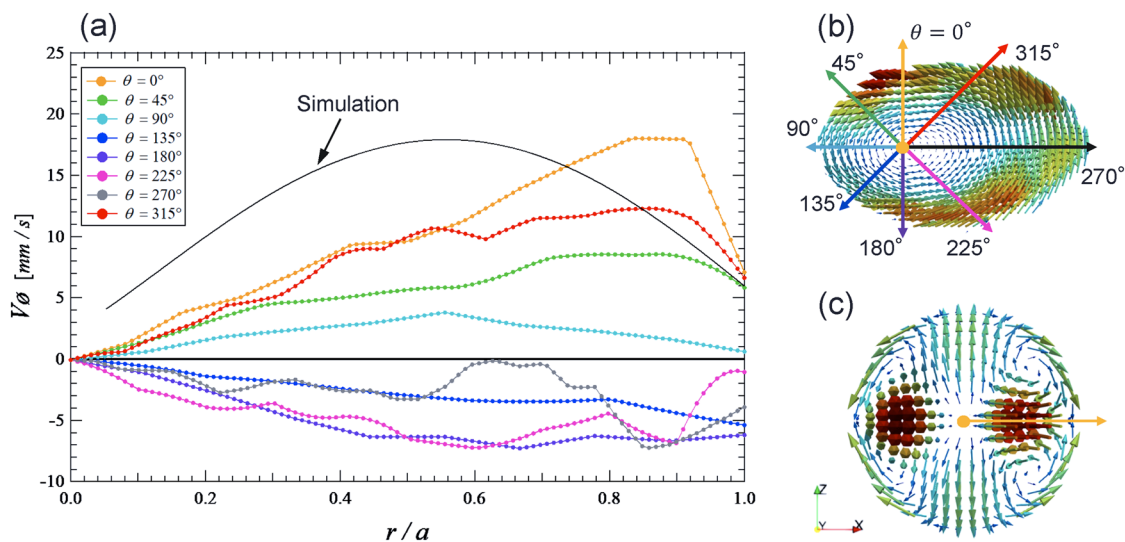


**FIG. 10.** Velocity distribution of circumferential component  $v_\theta$ : (a) comparison of analysis and experimental results, (b) measurement lines on vertical section of experimental result, and (c) a measurement line on the vertical section of analysis result when  $a = 1.44$  mm,  $U = 20.8$  mm/s,  $\omega = 14.4$  rad/s,  $A = 0.007$ , and  $B = 0.16$ .



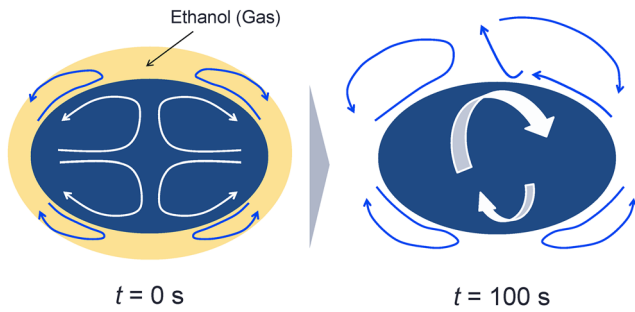


**FIG. 11.** Schematic of transition of internal and external flow structures of 50 wt. % ethanol droplet. The arrows indicate the direction of the internal and external flows.

rotation axis to the droplet interface with a different zenith angle  $\theta$ . The normalized distance in Fig. 10(a) is the distance from the rotation axis divided by the length from the axis to the interface, where  $r/a = 0$  represents the position of the rotation axis and  $r/a = 1$  represents the droplet interface. Note that the plots in Fig. 10(a) represent the experimental values. The measurement plane of each circumferential velocity distribution from the experimental results is defined in Fig. 10(b). One hundred circumferential velocity values between the origin (rotation center) and the droplet interface were obtained

with linear interpolation. With the same data processing, the velocity data at each angle from  $\theta = 0^\circ$  to  $315^\circ$  were acquired, as shown in Fig. 10(a), where the solid line represents the velocity distribution of the circumferential component between the rotation axis and the interface in the equatorial plane calculated by simulation with  $B = 0.16$ . Figure 10(c) shows the vertical section in the simulation result. Here, a half line is drawn from the rotation axis to the interface, as shown by the orange arrow in Fig. 10(c), and the circumferential velocity component on the half line is shown as the simulation result in Fig. 10(a).

Figure 10(a) confirms that the peak velocity distribution occurred around  $r/a = 0.9$ . This tendency is clearly observable at  $\theta = 0^\circ, 45^\circ,$  and  $315^\circ$ . In addition, the absolute value of the flow velocity at the top side (with  $\theta = 0^\circ, 45^\circ,$  and  $315^\circ$ ) of the droplet was generally larger than that of the bottom side (with  $\theta = 135^\circ, 180^\circ,$  and  $225^\circ$ ). Here, it is considered that the asymmetry in the upper and lower part of the droplet appeared because droplet was levitated and displaced slightly downward from the pressure node of the acoustic standing wave.

Based on the comparison of the present experimental and simulation result, the order of the peak velocity was well reproduced by analyzing in the order of  $O(Re^2)$ . For the water droplet, the internal flow structures demonstrated good agreement between the experimental and simulation results. In other words, the internal flow was driven by rotation of the acoustically levitated water droplet. It can

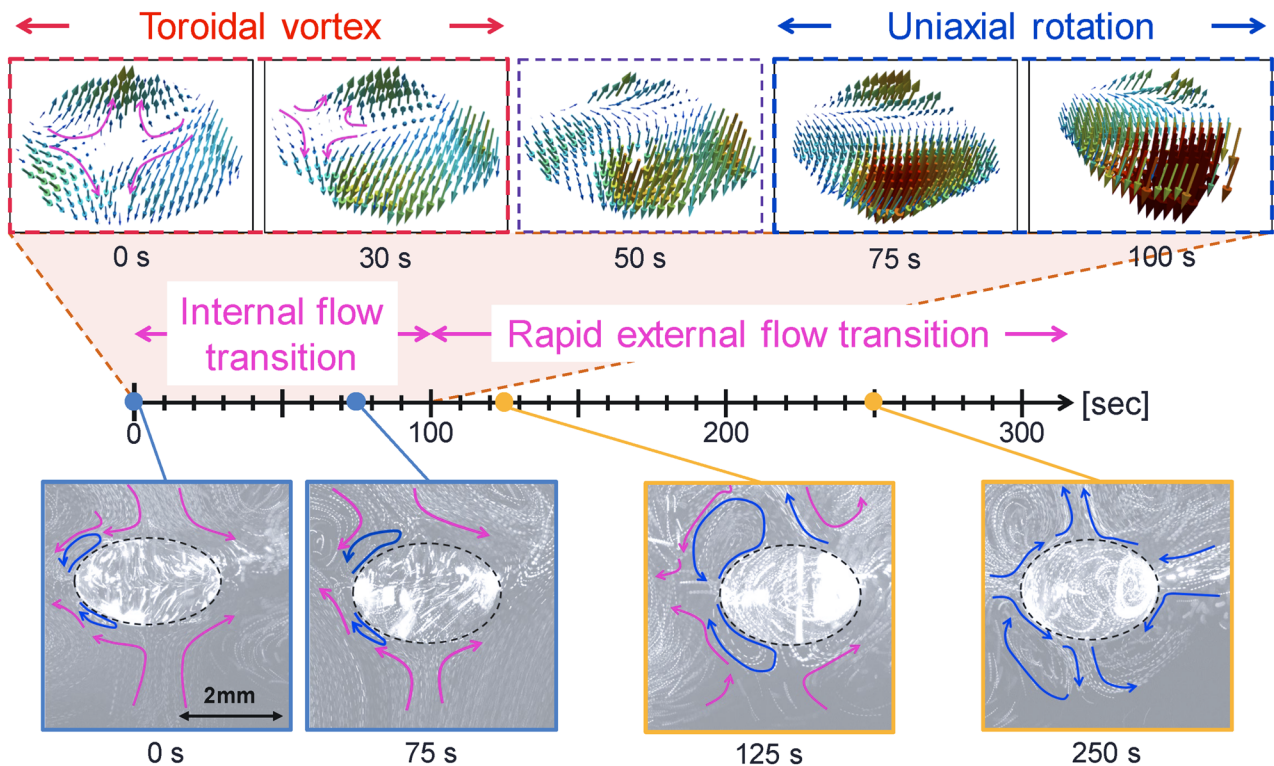


**FIG. 12.** Transition of internal and external flow structures of 50 wt. % ethanol droplet. For bottom four images, pink and blue arrows indicate the external flow structure and the circular vortex, respectively.

be inferred that the torque generated by the external flow caused this droplet rotation.

However, the distribution profile differed (the velocity peak of the experimental data was near the droplet interface) in experiment and simulation because stereo PIV does not consider the influence of refraction at the droplet interface. To address this problem, we plan to construct a calibration system that can correct the coordinate system while considering the effects of refraction.

#### IV. DISCUSSION

Here, based on the above results, the correlation between the internal/external flow fields and the evaporation behavior of the acoustically levitated droplet is discussed using the 50 wt. % ethanol case.

In Sec. III A, the visualization results of the transition process of the internal and external flow structures of 50 wt. % ethanol droplets were described. To obtain a deeper physical insight, Fig. 11 shows a schematic diagram of the internal and external flow structures immediately after levitation ( $t = 0$  s) and at  $t = 100$  s. In the vicinity of the droplet interface at  $t = 0$  s, the directions of the internal and external flows were completely opposite. Such a flow structure is qualitatively consistent with the theoretical prediction by Zhao *et al.*, who assumed the existence of a circulating flow in the Stokes boundary layer.<sup>19</sup> It is confirmed that there were no vertically symmetrical vortices inside the droplet, and a uniaxial rotational flow structure was generated at  $t = 100$  s. In addition, as shown in Fig. 6, symmetry breaking of the external flow structure appeared at the top and bottom due to the effect of gravity on the droplet position.

In Sec. III B, we simulated the internal flow of the rotating droplet, which demonstrated good agreement with our experimental result for the internal flow structure of the water droplet. We can infer that the dominant driving force when uniaxial rotational flow occurs in an acoustically levitated droplet could be the rotational torque due to the asymmetric external acoustic flow configuration.

Figure 12 summarizes the transition process of the internal and external flow structures with the evaporation progress of the 50 wt. % ethanol droplet. For the initial 100 s, during the expansion process of the circulating vortices, the asymmetry of the circulating vortices at the top and bottom of the droplet gradually increased. As this asymmetry of the external flow field strengthened, an external torque was exerted on the droplet interface. This may cause the internal flow transition from the same toroidal vortex structure (same as the pure ethanol droplet) to the uniaxial rotational flow (same as the pure water droplet). Around the transition of the internal flow, the external flow rapidly transitioned ( $t > 100$  s) by varying the concentration distribution of the ethanol vapor around the droplet.

#### V. CONCLUSION

We have applied Scheimpflug's theorem to high-speed cameras and succeeded in stereo visualization measurement of the internal and external flow of sound field floating droplets. We performed a visualization measurement of a 50 wt. % ethanol droplet using this method. In addition, we performed a detailed visualization measurement of the transition process of the internal and external

flows with evaporation. Both the internal and external flow fields demonstrated the same flow structure as the ethanol monolayer case immediately after levitation; however, over time, it was confirmed that they changed to the flow structure as the water monolayer. To perform a more detailed flow transition measurement on the time scale, the internal flow structure transitioned from a toroidal vortex structure to an uniaxial rotational flow structure between  $t = 0$ –100 s. In the external flow, focusing on the circulating vortices present at the top and bottom of the droplet immediately after floating, it was confirmed that it expanded rapidly after  $t = 100$  s. From this result, around the internal flow transition, the external flow rapidly transitioned ( $t > 100$  s) by changing the concentration distribution of the ethanol vapor around the droplet.

To clarify the driving mechanism of the uniaxial rotational flow structure, the flow generated inside the rotating droplet was simulated three-dimensionally based on Sano's theory. The internal flow of the water droplet obtained via stereo PIV was compared with it. As a result, the flow structures and the order of the velocity showed good agreement during simulation and experiment. From this, we have demonstrated that droplet rotation is dominant in the determination of the uniaxial rotational flow structure generated inside an acoustically levitated droplet.

These visualization measurements and simulations provide significant knowledge about the correlation between such internal and external flows, as well as the evaporation behavior of acoustically levitated droplets. In addition, knowledge about the influence of the rotation of the droplet itself on the internal flow structure was obtained. These findings are expected to contribute to the future development of fluid control technology via acoustic levitation. For applying the acoustic levitation in the drug discovery process, the phase change phenomena of fluids, such as evaporation and precipitation, should be accurately controlled.

#### ACKNOWLEDGMENTS

This work was supported by JSPS KAKENHI (Grant Nos. 16360097, 18360083, 23360081, and 15H03925). We thank Professor Katsuhiko Nishinari, Professor Tadashi Watanabe, Dr. Satoshi Matsumoto, Dr. Hiroyuki Kitahata, and Mr. Motonori Niwa for their insightful comments and suggestions. We would also like to acknowledge support from the Japan Aerospace Exploration Agency (JAXA).

#### REFERENCES

- <sup>1</sup>L. V. King, "On the acoustic radiation pressure on spheres," *Proc. R. Soc. London, Ser. A* **147**, 212 (1934).
- <sup>2</sup>A. L. Yarin, M. Pfaffenlehner, and C. Tropea, "On the acoustic levitation of droplets," *J. Fluid Mech.* **356**, 65 (1998).
- <sup>3</sup>E. H. Trinh and T. G. Wang, "Large-amplitude free and driven drop-shape oscillations: Experimental observations," *J. Fluid Mech.* **122**, 315 (1982).
- <sup>4</sup>V. Vandaele, P. Lambert, and A. Delchambre, "Non-contact handling in microassembly: Acoustical levitation," *Precis. Eng.* **29**, 491 (2005).
- <sup>5</sup>C. Bouyer, C. Pu, S. Güven, T. T. Demirtaş, T. J. F. Nieland, F. Padilla, and U. Demirci, "Bio-acoustic levitational (BAL) assembly method for engineering of multilayered, 3D brain-like constructs, using human embryonic stem cell derived neuro-progenitors," *Adv. Mater.* **28**, 161 (2016).
- <sup>6</sup>M. Sundvic, H. J. Nieminen, A. Salmi, P. Panula, and E. Häggström, "Effects of acoustic levitation on the development of zebrafish, *Danio rerio*, embryos," *Sci. Rep.* **5**, 13596 (2015).

- <sup>7</sup>T. Vasileiou, D. Foresti, A. Bayram, D. Poulikakos, and A. Ferrari, "Toward contactless biology: Acoustophoretic DNA transfection," *Sci. Rep.* **6**, 20023 (2016).
- <sup>8</sup>P. C. Nordine, D. Merkley, J. Sickel, S. Finkelman, R. Tell, A. Kaiser, and R. Prieler, "A levitation instrument for containerless study of molten materials," *Rev. Sci. Instrum.* **83**, 125107 (2012).
- <sup>9</sup>S. Rehder, J. X. Wu, J. Laackmann, H. Moritz, J. Rantanen, T. Rades, and C. S. Leopold, "A case study of real-time monitoring of solid-state phase transformations in acoustically levitated particles using near infrared and Raman spectroscopy," *Eur. J. Pharm. Sci.* **48**, 97 (2013).
- <sup>10</sup>D. Foresti, M. Nabavi, M. Klingauf, A. Ferrari, and D. Poliakos, "Acoustophoretic contactless transport and handling of matter in air," *Proc. Natl. Acad. Sci. U. S. A.* **110**, 12549 (2013).
- <sup>11</sup>A. Marzo, S. A. Seah, B. W. Drinkwater, D. R. Sahoo, B. Long, and S. Subramanian, "Holographic acoustic elements for manipulation of levitated objects," *Nat. Commun.* **6**, 8661 (2015).
- <sup>12</sup>Y. Ochiai, T. Hoshi, and J. Rekimoto, "Three-dimensional mid-air acoustic manipulation by ultrasonic phased arrays," *PLoS One* **9**, e97590 (2014).
- <sup>13</sup>A. Watanabe, K. Hasegawa, and Y. Abe, "Contactless fluid manipulation in air: Droplet coalescence and active mixing by acoustic levitation," *Sci. Rep.* **8**, 10221 (2018).
- <sup>14</sup>A. V. Anilkumar, C. P. Lee, and T. G. Wang, "Stability of an acoustically levitated and flattened drop: An experimental study," *Phys. Fluids A* **5**, 2763 (1993).
- <sup>15</sup>C. P. Lee, A. V. Anilkumar, and T. G. Wang, "Static shape and instability of an acoustically levitated liquid drop," *Phys. Fluids A* **3**, 2497 (1991).
- <sup>16</sup>Y. Tian, G. Holt, and R. E. Apfel, "Deformation and location of an acoustically levitated liquid drop," *J. Acoust. Soc. Am.* **93**, 3096 (1993).
- <sup>17</sup>Y. Abe, Y. Yamamoto, D. Hyuga, K. Aoki, and A. Fujiwara, "Interfacial stability and internal flow of a levitated droplet," *Microgravity Sci. Technol.* **19**, 33 (2007).
- <sup>18</sup>M. Kawakami, Y. Abe, A. Kaneko, and K. Hasegawa, "Effect of laser heating on nonlinear surface deformation of acoustically levitated droplet," *Mech. Sci. Technol.* **22**, 145 (2010).
- <sup>19</sup>H. Zhao, S. S. Sadhal, and E. H. Trinh, "Internal circulation in a drop in an acoustic field," *J. Acoust. Soc. Am.* **106**, 3289 (1999).
- <sup>20</sup>A. Y. Rednikov and S. S. Sadhal, "Steady streaming from an oblate spheroid due to vibrations along its axis," *J. Fluid Mech.* **499**, 345 (2004).
- <sup>21</sup>A. Y. Rednikov, H. Zhao, S. S. Sadhal, and E. H. Trinh, "Steady streaming around a spherical drop displaced from the velocity antinode in an acoustic levitation field," *Q. J. Mech. Appl. Math.* **59**, 377 (2006).
- <sup>22</sup>A. Y. Rednikov and S. S. Sadhal, "Acoustic/steady streaming from a motionless boundary and related phenomena: Generalized treatment of the inner streaming and example," *J. Fluid Mech.* **667**, 426 (2011).
- <sup>23</sup>K. Hasegawa, A. Kaneko, K. Aoki, and Y. Abe, "Simultaneous measurement of internal and external flow of an acoustically levitated droplet using PIV technique," *Jpn. J. Multiphase Flow* **23**, 523 (2010).
- <sup>24</sup>K. Hasegawa, A. Kaneko, K. Aoki, and Y. Abe, "PIV measurement of internal and external flow of an acoustically levitated droplet," *Int. J. Trans. Phenomena* **12**, 151 (2011).
- <sup>25</sup>K. Hasegawa, Y. Abe, A. Fujiwara, Y. Yamamoto, and K. Aoki, "External flow of an acoustically levitated droplet," *Microgravity Sci. Technol.* **20**, 261 (2008).
- <sup>26</sup>K. Hasegawa, Y. Abe, A. Fujiwara, Y. Yamamoto, and K. Aoki, "Visualization measurement of streaming flows associated with a single-acoustic levitator," *Microgravity Sci. Technol.* **21**, S9 (2009).
- <sup>27</sup>Y. Yamamoto, Y. Abe, A. Fujiwara, K. Hasegawa, and K. Aoki, "Internal flow of acoustically levitated droplet," *Microgravity Sci. Technol.* **20**, 277 (2008).
- <sup>28</sup>Z. L. Yan, W. J. Xie, and B. Wei, "Vortex flow in acoustically levitated drops," *Phys. Lett. A* **375**, 3306 (2011).
- <sup>29</sup>K. Shitanishi, K. Hasegawa, A. Kaneko, and Y. Abe, "Study on heat transfer and flow characteristic under phase-change process of an acoustically levitated droplet," *Microgravity Sci. Technol.* **26**, 305 (2014).
- <sup>30</sup>M. Niwa, A. Goda, K. Hasegawa, T. Kanagawa, A. Kaneko, and Y. Abe, "Effect of temperature change on internal-external flow and convective heat transfer of an acoustically levitated droplet," *Jpn. J. Multiphase Flow* **29**, 501 (2016).
- <sup>31</sup>A. L. Yarin, G. Brenn, O. Kastner, D. Rensink, and C. Tropea, "Evaporation of acoustically levitated droplets," *J. Fluid Mech.* **399**, 151 (1999).
- <sup>32</sup>A. L. Yarin, G. Brenn, O. Kastner, and D. Rensink, "Evaporation of acoustically levitated droplets of binary liquid mixtures," *Int. J. Heat Fluid Flow* **23**, 471 (2002).
- <sup>33</sup>G. Brenn, L. J. Deviprasath, F. Durst, and C. Fink, "Evaporation of acoustically levitated multi-component liquid droplets," *Int. J. Heat Mass Transfer* **50**, 5073 (2007).
- <sup>34</sup>K. Kobayashi, A. Goda, K. Hasegawa, and Y. Abe, "Flow structure and evaporation behavior of an acoustically levitated droplet," *Phys. Fluids* **30**, 082105 (2018).
- <sup>35</sup>K. Hasegawa, A. Goda, and Y. Abe, "Microlayered flow structure around an acoustically levitated droplet under a phase-change process," *npj Microgravity* **2**, 16004 (2016).
- <sup>36</sup>Y. Niimura and K. Hasegawa, "Evaporation of droplet in mid-air: Pure and binary droplets in single-axis acoustic levitator," *PLoS One* **14**(2), e0212074 (2019).
- <sup>37</sup>A. Goda, K. Hasegawa, A. Kaneko, T. Kanagawa, and Y. Abe, "External flow structure and interfacial transport phenomena of an acoustically levitated droplet," *Jpn. J. Multiphase Flow* **28**, 539 (2015).
- <sup>38</sup>E. Bänsch and M. Götz, "Numerical study of droplet evaporation in an acoustic levitator," *Phys. Fluids* **30**, 037103 (2018).
- <sup>39</sup>H. Ishii, K. Hasegawa, A. Kaneko, and Y. Abe, "Internal and external flow structure and mass transport phenomena of an acoustically levitated droplet," *Trans. Jpn. Soc. Mech. Eng., Ser. B* **78**, 1696 (2012).
- <sup>40</sup>O. Sano, "Flow and deformation in rotating droplets (prospects for mathematical fluid dynamics)," *RIMS Kokyuroku* **922**, 124 (1995) [in Japanese].
- <sup>41</sup>Z. Chen, D. Zang, L. Zhao, M. Qu, X. Li, X. Li, L. Li, and X. Geng, "Liquid marble coalescence and triggered microreaction driven by acoustic levitation," *Langmuir* **33**, 6232 (2017).
- <sup>42</sup>A. Marzo and B. W. Drinkwater, "Holographic acoustic tweezers," *Proc. Natl. Acad. Sci. U. S. A.* **116**(1), 84 (2018).
- <sup>43</sup>S. Walker, "Two-axes Scheimpflug focusing for particle image velocimetry," *Meas. Sci. Tech.* **13**, 1 (2002).
- <sup>44</sup>E. W. Lemmon, M. L. Huber, and M. O. McLinden, NIST Standard Reference Database 23, version 9.0, 2013.